

Coseismic fault slip associated with the 1992 M_w 6.1 Joshua Tree, California, earthquake: Implications for the Joshua Tree-Landers earthquake sequence

Richard A. Bennett, Robert E. Reilinger, William Rodi, Yingping Li, and M. Nafi Toksöz

Earth Resources Laboratory, Department of Earth, Atmospheric, and Planetary Sciences
Massachusetts Institute of Technology, Cambridge

Ken Hudnut

U.S. Geological Survey, Pasadena, California

Abstract. Coseismic surface deformation associated with the M_w 6.1, April 23, 1992, Joshua Tree earthquake is well represented by estimates of geodetic monument displacements at 20 locations independently derived from Global Positioning System and trilateration measurements. The rms signal to noise ratio for these inferred displacements is 1.8 with near-fault displacement estimates exceeding 40 mm. In order to determine the long-wavelength distribution of slip over the plane of rupture, a Tikhonov regularization operator is applied to these estimates which minimizes stress variability subject to purely right-lateral slip and zero surface slip constraints. The resulting slip distribution yields a geodetic moment estimate of 1.7×10^{18} N m with corresponding maximum slip around 0.8 m and compares well with independent and complementary information including seismic moment and source time function estimates and main shock and aftershock locations. From empirical Green's function analyses, a rupture duration of 5 s is obtained which implies a rupture radius of 6–8 km. Most of the inferred slip lies to the north of the hypocenter, consistent with northward rupture propagation. Stress drop estimates are in the range of 2–4 MPa. In addition, predicted Coulomb stress increases correlate remarkably well with the distribution of aftershock hypocenters; most of the aftershocks occur in areas for which the mainshock rupture produced stress increases larger than about 0.1 MPa. In contrast, predicted stress changes are near zero at the hypocenter of the M_w 7.3, June 28, 1992, Landers earthquake which nucleated about 20 km beyond the northernmost edge of the Joshua Tree rupture. Based on aftershock migrations and the predicted static stress field, we speculate that redistribution of Joshua Tree-induced stress perturbations played a role in the spatio-temporal development of the earthquake sequence culminating in the Landers event.

Introduction

The M_w 6.1, April 23, 1992, Joshua Tree, California, earthquake resulted from right-lateral rupture along a previously unmapped north trending late Quaternary fault located about 20 km south of the Pinto Mountain fault and about 10 km northeast of the Mission Creek branch of the San Andreas fault system (Figures 1 and 2). This and other subparallel late Quaternary faults, identified following the earthquake, offset an older northwest trending system [Rymer, 1992].

Seismicity here is characterized by frequent earthquake swarms suggesting that faults in the area are immature [Hauksson *et al.*, 1993]. It is also the location of a sequence of moderate earthquakes occurring between 1940 and 1948 [Richter *et al.*, 1958; Sykes and Seeber, 1985] which included the 1940 M_L 5.3 Covington Flat, 1947 M_L 5.4 Morongo Valley, and 1948 M_L 6.5 Desert Hot Springs earthquakes. The Covington Flat earthquake likely involved rupture along one of these north trending faults, possibly the same fault ruptured during the Joshua Tree earthquake.

These north trending faults lie in what is known as the Eastern California Shear Zone (ECSZ) [Dokka and Travis, 1990a], a zone of intracontinental right-lateral shear bordering the southern San Andreas fault system to the east and extending northwestward through

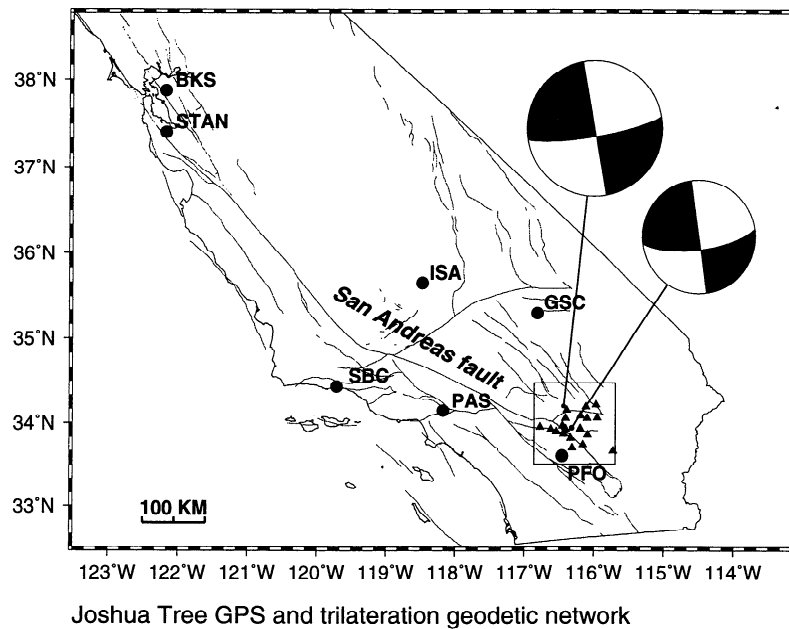


Figure 1. Simplified fault map showing the location of the GPS and trilateration monuments (triangles) in the vicinity of the 1992 Joshua Tree earthquake in southern California. Also shown (dots) are the locations of the seismic stations used for the empirical Green's functions analysis. Focal mechanisms from *Hauksson et al.* [1993] are shown for the Joshua Tree (southern event) and Landers (northern event) earthquakes. The square around the geodetic monuments shows the location of Figure 2.

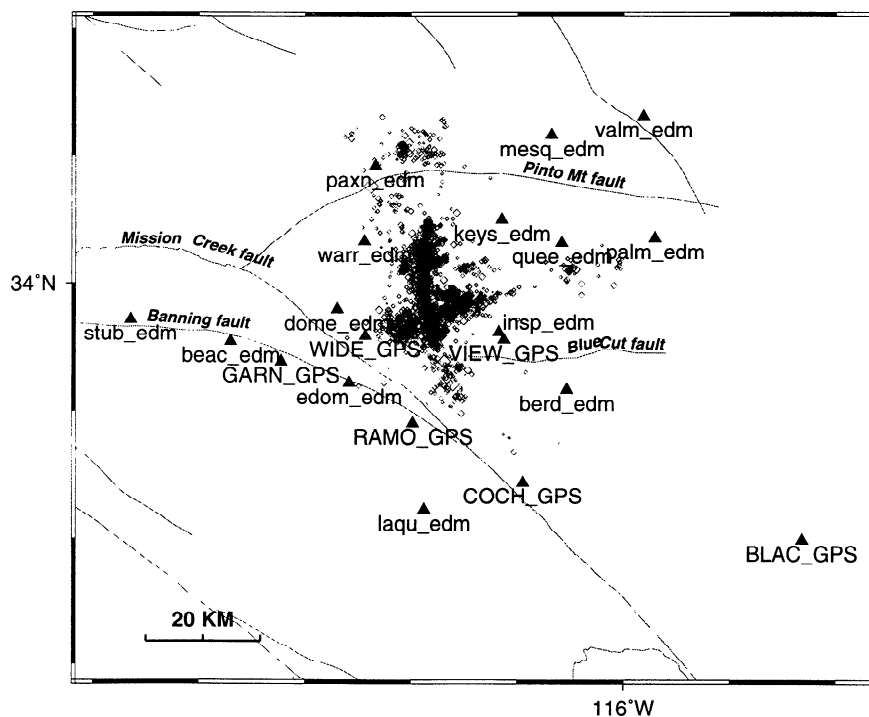


Figure 2. Map showing location of the geodetic stations (triangles) in relation to the 1992 Joshua Tree earthquake. Aftershocks from *Hauksson et al.* [1993] are shown as diamonds. The large diamond northwest of site paxn shows the location of the Landers epicenter.

the Mojave Desert and on into Death Valley. Geologic and geodetic evidence [Sauer *et al.*, 1986; Dokka and Travis, 1990b; Savage *et al.*, 1990] suggests that 9 to 23% of the total Pacific-North American relative plate motion is accommodated within this zone. However, Savage *et al.* [1990] found that the strain rate is too large to be regionally distributed and inferred the existence of a localized zone of shear controlled by "some flaw in the lithosphere," noting further that local north-west trending faults do not serve this purpose because their traces are not easily reconciled with observed principal strain axes. One intriguing idea, proposed by Nur *et al.* [1992], is that the Joshua Tree and Landers earthquakes belong to a series of events all occurring along a new fault trending N10°W and extending roughly 100 km across the Mojave desert.

The Joshua Tree earthquake preceded by nearly 2 months the M_w 7.3 Landers earthquake, southern California's largest earthquake in 40 years. The distance between hypocenters for these earthquakes is near 30 km, and both events involved rupture along roughly the same north trending plane within the ECSZ. However, while the Landers earthquake resulted in spectacular surface ruptures extending about 85 km in length, no surface rupture was observed for the Joshua Tree event [Rymer, 1992]. This is unfortunate in that detailed knowledge of the two-dimensional distribution of slip is prerequisite to accurate calculation of coseismic stress transfer and investigation of its implications for the temporal development of the Joshua Tree-Landers earthquake sequence.

Fortunately, coseismic deformation associated with this event is well represented by estimates of geodetic monument displacements at 20 locations (Figure 2) derived from preearthquake and postearthquake observations. These observations consist of Global Positioning System (GPS) measurements collected between February 1990 and April 1992 together with trilateration measurements collected since 1973 [e.g., Savage *et al.*, 1993]. In this paper, results of analyses of these geodetic data are presented with primary focus on estimates for displacements associated with the Joshua Tree event. Employing a simple dislocation model and an inversion method based on Tikhonov regularization, these estimates are used to infer the long-wavelength distribution of slip associated with this event. The size, shape, and location of the resulting slip distribution are then checked against main shock and aftershock locations and seismic moment and source time function estimates. These independent observations serve not only to constrain many of the important features of the slip distribution but also provide complimentary information facilitating a more complete seismotectonic analysis. By integrating seismic and geodetic information, we attempt to resolve possible complexities of the Joshua Tree rupture process and to assess the significance of coseismic stress transfer in the spatio-temporal evolution of earthquake activity following this event.

Geodetically Derived Model of Fault Slip

Coseismic Surface Deformation

Trilateration. The U.S. Geological Survey has been monitoring deformation in the vicinity of the Joshua Tree earthquake by trilateration since 1973 (Figure 2). Measurements include pre- and post-Joshua Tree earthquake observations and provide estimates of the coseismic displacements associated with the event. Savage *et al.* [1993] investigated deformation of this network associated with the earthquake and found that it is compatible with slip on a buried 7×12 km² rectangular fault with strike of 353°, dip of 90°, and moment of 1.8×10^{18} N m. Geodetic estimates for coseismic deformation were not reported in this study, but estimates for coseismic displacement at 14 sites (Figure 2) from these same trilateration data are provided by Dong [1993]. Dong's displacement estimates are incorporated in the present study.

GPS. GPS measurements were initiated in the Joshua Tree earthquake region in 1988 with reobservation campaigns in 1990, 1991, and 1993 [Reilinger and Larsen, 1993]. For the purposes of determining ground motions prior to the Joshua Tree earthquake, the observations made during 1990 and 1991 are of primary importance. Because preliminary analysis of the original 1988 data has proved difficult due to problems in the time tagging of the recorded phase observations, these data were not considered for the present study. Furthermore, all observations subsequent to the June 28, 1992, Landers earthquake, namely, the 1993 survey, are of limited help in recovering deformation associated with the Joshua Tree event due to the large Landers signal [e.g., Murray *et al.*, 1993]. Additional preearthquake observations were made from a small subset of stations on April 13, 16, and 21, 1992. Postearthquake observations were collected between April 25 and 28 in response to the Joshua Tree earthquake. Using these four observation sets (1990, 1991, 1992 preearthquake, and 1992 postearthquake), we obtained coseismic displacement estimates for six GPS stations (Figure 2) that were observed at least twice prior to and once following the earthquake (Table 1).

In our analyses, we combined the GPS phase observations from these sites with all available global tracking using the GAMIT/GLOBK software as described by Feigl *et al.* [1993]. We obtained secular site velocity estimates (1990–1992 preearthquake) from analysis of all preearthquake GPS measurements. We included observations collected from an additional GPS monument (PIN1) here for comparison with geological estimates of slip rates across the southern San Andreas fault. Velocity estimates computed with respect to station BLAC are shown in Figure 3. Despite the short duration between experiments, errors are sufficiently small to reveal right-lateral motion about the San Andreas Fault.

Table 1. Site Observation History

	COCH	GARN	RAMO	VIEW	WIDE	BLAC	PIN1
1990	*	*	*	*	*	*	*
1991	*	*	*	*	*	*	*
1992 pre		*				*	*
1992 post	*	*	*	*	*	*	*

These data are consistent with strictly secular deformation in the years prior to the earthquake as inferred from 19 years of trilateration measurements [Savage *et al.*, 1993]. A screw dislocation model assuming a locking depth of 15 km and slip rate of 28 mm/yr for the southern San Andreas compares well with the relative velocities between sites BLAC and PIN1 (Figure 4). This result is consistent with geological estimates of slip rate along this segment of the San Andreas of 23–35 mm/yr with commonly accepted nominal value of 25 mm/yr [Sieh and Williams, 1990; Sieh *et al.*, 1989]. The most important aspect of the velocity field from the point of view of this analysis is, however, that the relative secular motions among most of the GPS sites in the vicinity of the Joshua Tree earthquake are quite small. Hence we do not expect errors in our velocity estimates to translate into significant coseismic displacement estimate errors.

Finally, we used the FONDA software package [Dong, 1993] to estimate coseismic displacements and preearthquake velocities simultaneously from all four GPS observation sets. The resulting coseismic displacement estimates have a root-mean-square (rms) signal of 15 mm and error of 5 mm giving an rms signal-to-noise ratio of about 3.0. These displacement estimates, together with the trilateration estimates of Dong [1993], shown in Plate 1), form the basis of this study. The combined GPS and trilateration set consists of 40 displacements

(two components of horizontal displacement for each of the 20 geodetic stations) with rms signal of 20 mm and error of 11 mm giving an rms signal-to-noise ratio of about 1.8.

Modeling the Joshua Tree Earthquake

Since its introduction in 1958, the elasticity theory of dislocations [Steketee, 1958a,b] has been one of the most commonly used formalisms for studies of the earthquake source. The model relates a distributed displacement discontinuity $\Delta u = (\Delta u_1, \Delta u_2, \Delta u_3)$ across a surface Σ to the resultant static displacement $u = (u_1, u_2, u_3)$ at a point $r = (x_1, x_2, x_3)$ in an elastic medium \mathcal{E} . This is the Volterra integral [e.g., Aki and Richards, 1980]

$$u_p(r) = \frac{1}{8\pi\mu} \int \int_{\Sigma} \Delta u_j(\xi) w_{jk}^p(r, \xi) \nu_k(\xi) d\Sigma(\xi),$$

$$p = 1, 2, 3 \quad (1)$$

where μ is the rigidity in the source region, ν is the normal vector to the dislocation surface Σ , and w_{jk}^p is an appropriate Green's tensor. Analytic solutions for this integral have been obtained for the case when Δu is constant and \mathcal{E} is a homogeneous, isotropic, linearly elastic half-space given a number of dislocation geometries [e.g., Chinnery, 1961; Savage and Hastie, 1966; Mansinha and Smylie, 1971; Okada, 1985]. For the case of a layered half-space, complete expressions for the

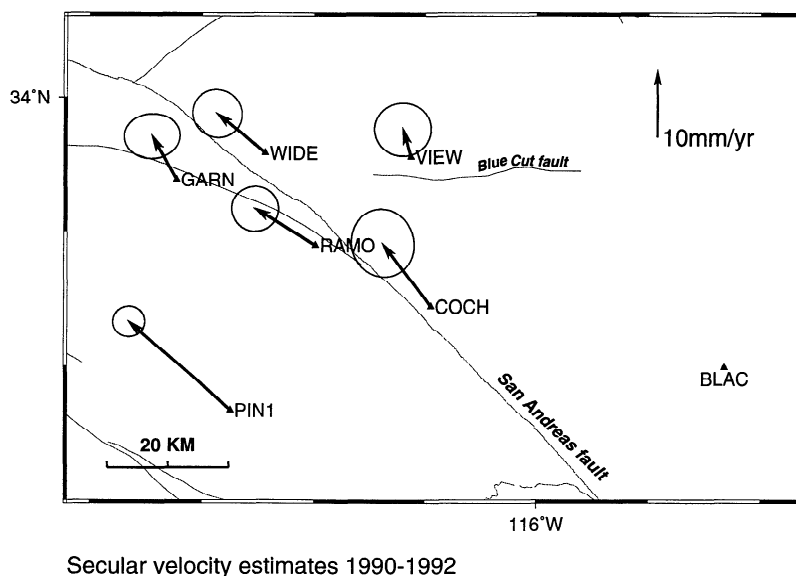
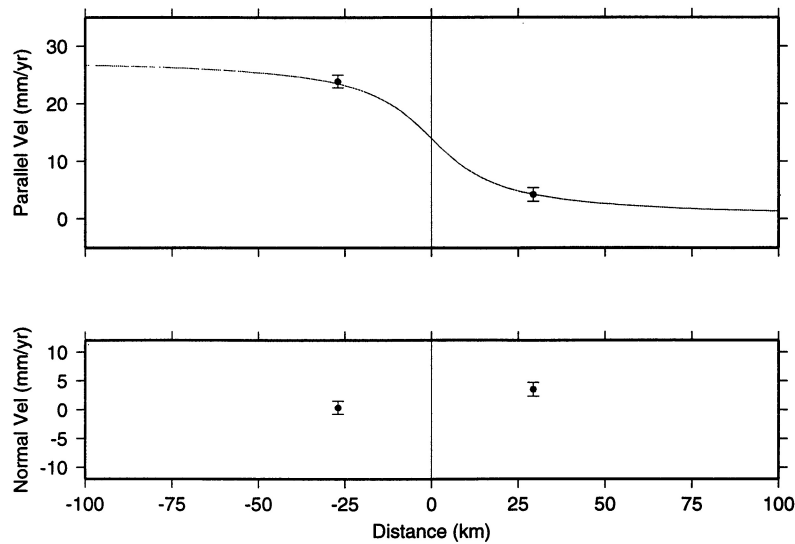


Figure 3. Secular velocities (arrows) estimated from GPS observations spanning 1990–1992. Velocities are shown relative to site BLAC (lower right corner). Error ellipses indicate 95% confidence level.



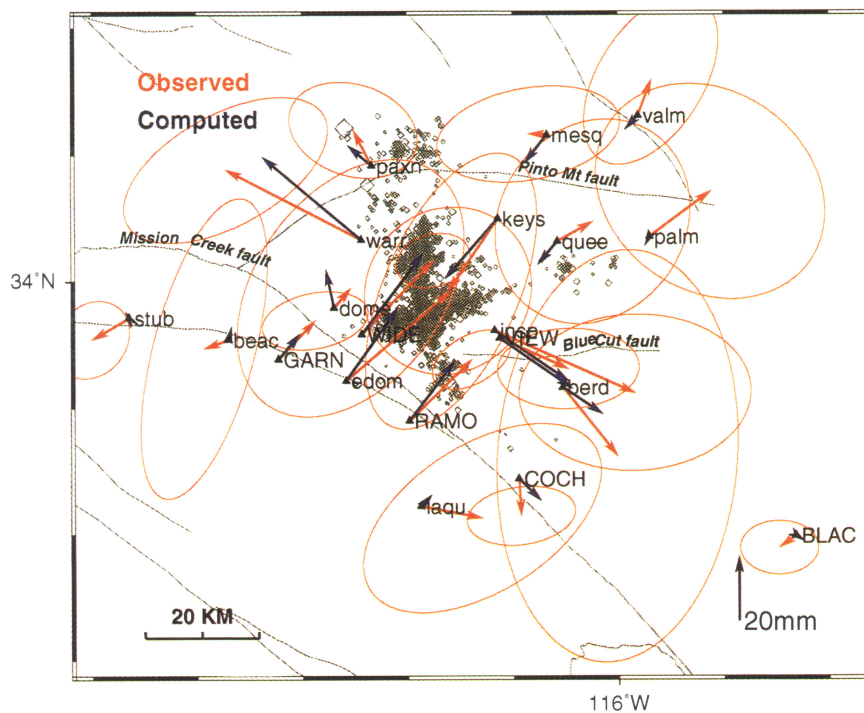
Screw Dislocation Velocity Model:
 One sigma error bars (scaled by 1.00)
 Locking depth: 15.0 km
 Slip Rate: 28 mm/yr

Figure 4. Screw dislocation velocity model for the southern San Andreas fault (15 km locking depth, 28 mm/yr slip rate) together with GPS velocities for sites BLAC (right point) and PIN1 (left point). GPS errors are one standard deviation.

w_{jk}^p together with efficient numerical computation techniques have been developed [Ben-Menahem and Singh, 1968; Ben-Menahem and Gillon, 1970; Singh, 1970; Jovanovich et al., 1974a].

In the present study, the model is applied with the

dislocation representing the two-dimensional surface of the ruptured fault plane within Earth. Since the effects of Earth's curvature are negligible over distances of less than about 2000 km [Ben-Menahem et al., 1970], a half-space model is sufficiently accurate for the present



23 April 1992 Joshua Tree Earthquake

Plate 1. Geodetically observed (red) and model predicted (blue) horizontal displacements. GPS sites are indicated by all capital site names. Trilateration sites are indicated by all lowercase site names. Ninety-five percent confidence level error ellipses are shown for observed displacements.

study. Several studies [e.g., *Jovanovich et al.*, 1974b; *Savage*, 1987] suggest that the effects of layering in rigidity within Earth over distance scales comparable to those of this study and under nominal crustal conditions are small relative to homogeneous half-space models. In fact, for the case of a Poisson solid, (1) is independent of the rigidity [e.g., *Okada*, 1985]. The daily scatter in the postearthquake observations suggests that post-seismic motions are not detected and hence nothing is gained by including time dependent deformation effects save perhaps a minimal adjustment to the estimated amplitude; a linearly elastic model should thus suffice.

Focal mechanism estimates indicate right-lateral, almost purely strike-slip motion along a steeply dipping rupture plane striking at about 352° [*Incorporated Research Institutions for Seismology* (IRIS), 1992]. Accordingly, we restrict our model to pure right-lateral, strike-slip motion. We also assume a vertical dislocation plane based on the results of *Hauksson et al.* [1993] and *Savage et al.* [1993]. We define our coordinate system such that Σ is in the x_1 - x_3 plane, where x_3 is depth and x_1 is distance along the strike direction (x_2 is normal to Σ). The restriction to purely strike-slip motion reduces the three-vector Δu to the form $\Delta u = (s, 0, 0)$, where s is a scalar slip function. The assumption of right-lateral motion implies that s is of one sign and by convention is defined positive giving $s(\xi) \geq 0$ for all $\xi \in \Sigma$.

No surface rupture has been observed [*Rymer*, 1992] but the conjugate distribution of aftershock epicenters occurring between April and June 1992 [*Hauksson et al.*, 1993] forms a cross marking the event's general location (Figure 2). The horizontal location of the dislocation centroid is assumed to be roughly the center of the aftershock pattern as determined by eye. The lateral and depth extent of the component of the rupture centroid in the plane of the dislocation need not be specified as it will be determined by the data. This is insured by extending the edges of the dislocation surface laterally and in depth so as to render the effects of the boundary conditions on these edges negligible.

The geodetic observations described above provide estimates of the horizontal components of coseismic surface displacement u at various locations. The i th datum, denoted y_i , is thus $y_i = u_{p_i}(r_i)$, where r_i is the location of one of the geodetic monuments and $p_i = 1$ or 2. Given these specifications, equation (1) can be used to relate N such data to the slip function s as

$$y_i = \int_{\Sigma} g_i(\xi) s(\xi) d\Sigma(\xi) + \eta_i, \quad i = 1, 2, \dots, N \quad (2)$$

where, from (1), the functions g_i are given by

$$g_i(\xi) = \frac{1}{8\pi\mu} w_{12}^{p_i}(r_i, \xi), \quad (3)$$

and the η_i are the a posteriori errors in the estimates y_i obtained during the geodetic data reductions. By defining N linear functionals G_i as

$$G_i(s) = \int_{\Sigma} g_i(\xi) s(\xi) d\Sigma(\xi), \quad i = 1, 2, \dots, N, \quad (4)$$

equation (2) can be written more concisely as

$$y_i = G_i(s) + \eta_i. \quad (5)$$

Observations of zero surface slip [*Rymer*, 1992] are incorporated by assuming M discrete measurements, b_i , of zero slip at several locations along the intersection of the dislocation plane with the surface of the half-space. This information is included in the analysis via the equations

$$b_i = \delta_{\xi_i} s + \epsilon_i, \quad i = 1, 2, \dots, M \quad (6)$$

where the ϵ_i are assumed errors in the observations of the surface slip and δ_{ξ_i} are the point evaluation functionals, $\delta_{\xi_i} s = s(\xi_i)$ for a set of M points ξ_i on the edge of the dislocation plane along the half-space surface. A rather large variance of $E\epsilon_i\epsilon_i = (30 \text{ mm})^2$ is assigned to these pseudo-data.

By letting

$$d = (y_1, \dots, y_N, b_1, \dots, b_M). \quad (7)$$

$$e = (\eta_1, \dots, \eta_N, \epsilon_1, \dots, \epsilon_M), \quad (8)$$

and

$$A = (G_1, \dots, G_N, \delta_{\xi_1}, \dots, \delta_{\xi_M}), \quad (9)$$

equations (5) and (6) can be written together concisely as

$$d = As + e. \quad (10)$$

Inverse Theory

The use of geophysical data to infer distributed earthquake slip has been studied and demonstrated by several investigators using a variety of approaches [e.g., *Hartzell and Heaton*, 1983; *Ward and Barrientos*, 1986; *Segall and Harris*, 1987; *Mendoza and Hartzell*, 1988; *Matthews*, 1991; *Larsen et al.*, 1992; *Du et al.*, 1992; *Wald and Heaton*, 1994]. The strategy adopted for this analysis incorporates ideas discussed by *Matthews* [1991] and *Du et al.* [1992].

We would like to use (10) to infer the slip function s . However, it is clear that even exact measurements of the surface displacements resulting from the earthquake are not sufficient to determine the slip function uniquely using (10) alone since the continuous slip function is infinite dimensional. An approximate representation of s that is unique and stable under small perturbations to the data must suffice. A family of such approximations can be constructed by exploiting prior knowledge about the slip function and by minimization of a physically motivated, sufficiently stabilizing functional. This procedure is most conveniently carried out in a Hilbert space setting.

We assume that the data errors e_i are zero mean random variables and let V denote their known variance-

covariance matrix (i.e., $V_{ij} = E e_i e_j$). We then let \mathcal{D} be the Hilbert space of data vectors defined by the linear space \mathbb{R}^{N+M} under the norm

$$\|d\|_{\mathcal{D}}^2 = \sum_{i,j=1}^{N+M} V_{ij}^{-1} d_i d_j \quad (11)$$

where V^{-1} is the inverse of V .

Our objective is to find a slip function s subject to the following three constraints:

1. The geodetic misfit, or weighted residual sum of squares $\chi^2 \equiv \sum_{i,j=1}^N V_{ij}^{-1} \Delta y_i \Delta y_j$ (where the $\Delta y_i = y_i - G_i(s)$ are the residuals), should be consistent with the given variance-covariance matrix of the errors η_i in the geodetic data.

2. Among competing models satisfying constraint 1, the solution should, in some sense, have minimal structure. For our problem, a suitable measure is given by the functional $\int_{\Sigma} [\nabla^2 s(\xi)]^2 d\Sigma(\xi)$. This choice is particularly satisfying since, as shown by *Matthews* [1991], it is a good approximation to a measure of fault surface traction variability and therefore provides a physical basis for our minimization criterion. Matthews coined the term “stress variability” norm for this functional.

3. The model must allow only right-lateral slip. This translates into the positivity constraint $s(\xi) \geq 0$ for each $\xi \in \Sigma$.

We employ the method of Tikhonov regularization [*Tikhonov and Arsenin*, 1977] to achieve this objective.

We define the real valued functional Ψ_{α} for each $\alpha > 0$ as

$$\Psi_{\alpha}(s; d) = \|d - As\|_{\mathcal{D}}^2 + \alpha^2 \Omega(s) \quad (12)$$

where the stabilizing functional $\Omega(s)$ represents the “stress variability” functional together with homogeneous boundary conditions for s on $\partial\Sigma$:

$$\Omega(s) = \int_{\Sigma} [\nabla^2 s(\xi)]^2 d\Sigma(\xi) + \int_{\partial\Sigma} s(\xi)^2 d\sigma(\xi). \quad (13)$$

Constraints 1 and 2 are satisfied by minimization of Ψ_{α} over a suitable space of slip functions \mathcal{S}_+ and careful selection of the regularization parameter α . In other words, we define the solution s_{α} by

$$\Psi_{\alpha}(s_{\alpha}; d) = \inf_{s \in \mathcal{S}_+} \Psi_{\alpha}(s; d), \quad (14)$$

such that constraint 1 is true. For \mathcal{S}_+ , we use the space of positive functions on Σ with square integrable second order derivatives. This choice insures constraint 3.

Owing to the positivity constraint and the properties of the point evaluation functionals, we must appeal to a rather general formulation of regularization due to *Morozov* [1993]. It is not difficult to show that Morozov’s conditions for the existence and uniqueness of the solution s_{α} are satisfied for our problem for arbitrary d and $\alpha > 0$. We can thus write

$$s_{\alpha} = R(d, \alpha), \quad (15)$$

where R is known as the regularization operator.

Numerical Prescription

To numerically compute a solution the model is discretized on a 1 km square grid. The slip function s is assumed to be constant on each of the resulting 1 km square fault elements. The forward problem then reduces to a matrix equation with well known analytic expressions for the elements of the discretized g_i [e.g., *Chinnery*, 1961; *Okada*, 1985]. The number of assumed observations of surface slip, M , is chosen such that we have one data point per surface fault element. Discretization of the stabilizing functional Ω yields a functional of the form $(Ls)^T Ls$, where the matrix L is a difference operator. Finally, two sets of bias parameters representing rigid body translations of the GPS and trilateration observations were added to resolve indeterminacy and align the displacement estimate sets within the dislocation reference frame.

Program NNLS of *Lawson and Hanson* [1974] was then used to obtain solutions to the discrete problem. This algorithm is very convenient and efficient and has been successfully applied to problems of slip determination by numerous investigators: *Hartzell and Heaton* [1983] using strong motion waveforms, *Mendoza and Hartzell* [1988] using teleseismic waveforms, and *Du et al.* [1992] using static ground displacements.

Goodness of Fit and Selection of the Regularization Parameter

The regularization procedure outlined above provides a means of computing a family of solutions which approximately minimize the variability of fault surface traction. Increasing the regularization parameter α leads to smoother models (i.e., more uniform slip over the dislocation), while decreasing α allows more structure into the distribution (Figure 5). As mentioned

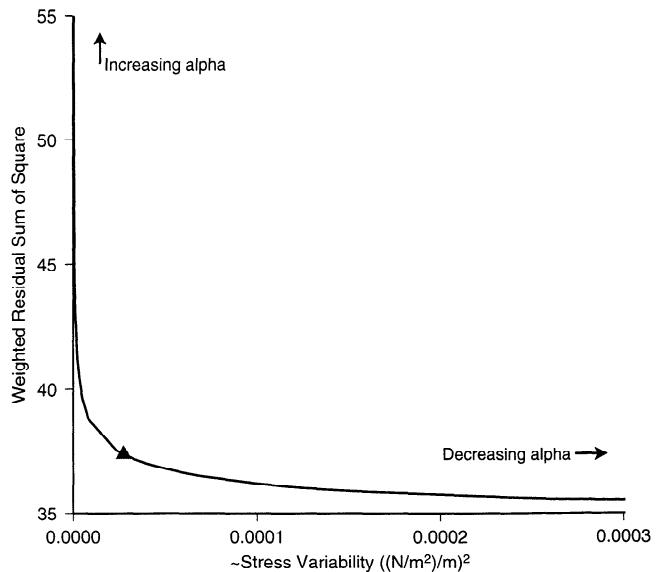


Figure 5. Stress variability versus data misfit trade-off curve. Triangle shows the location on the curve corresponding to the inferred model. Increasing the regularization parameter leads to smoother models (and correspondingly poorer fit to the data), while decreasing this parameter leads to more complex models (and correspondingly better fit to the data).

above, we look for the least complicated model such that the geodetic misfit is consistent with our a priori knowledge of the geodetic data errors. This corresponds to the “discrepancy” method for selecting α [Tikhonov and Arsenin, 1977].

In standard statistical least squares it is common practice to obtain an a posteriori estimate of the data variance. However, such estimates are difficult to obtain from regularized inversions due to the fact that s_α is a biased estimator when $\alpha > 0$. While approximate methods exist for obtaining the number of degrees of freedom and a posteriori variance (Wahba, 1990), we know of no such method which accounts for nonlinearity. Rather than naively applying an existing methodology, we opted simply to verify the consistency of the misfits and a priori uncertainties by performing numerical experiments.

We began by assuming a test value of the regularization parameter. We then applied the regularization operator to the geodetic data to obtain a model for slip. We generated reference displacements at each of the geodetic stations using this reference model and simulated observations by adding noise to these reference displacements. The noise processes used had a variance-covariance matrix of the form of the given error variance-covariance matrix times a scale factor σ^2 . We performed several inversions using several realizations for various values of σ^2 , again using the same test value of the regularization parameter. In this way we obtain the probability distribution of misfit as a function of σ^2 . By comparing the reference model misfit to the means of the simulated distributions, we obtain an a posteriori estimate of σ^2 . This method is analogous to the usual a posteriori variance estimate in linear least squares, where the probability distribution is known to be chi-square with number of degrees of freedom equal to the rank of the system matrix.

For large values of the regularization parameter, we obtain a variance scale factor greater than one, indicating that the resulting residuals have a scatter more consistent with a larger variance than that used in the inversion. For smaller values of the regularization parameter, we obtain a variance scale factor less than one, indicating that we are fitting the data better than the assumed variance of the data requires. The discrepancy method is, then, to select the value of the regularization parameter α that yields $\sigma^2 = 1$. Figure 6 shows the simulation for our preferred value of regularization parameter. We see that for this value of α , the solution weighted residual sum of squares indeed implies that $\sigma^2 = 1$. All solutions presented below were obtained using this preferred value of the regularization parameter.

Plate 1 shows the fit of the model to the site displacements. Table 2 lists the site displacements and postfit residuals. Since our data and their uncertainties were derived from two independent analyses (GPS displacements from this study; trilateration displacements

Discrepancy

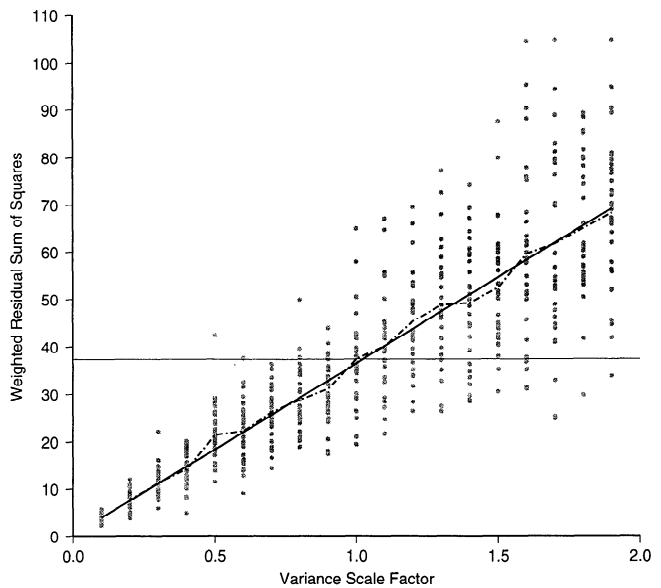


Figure 6. Geodetic misfit χ^2 versus variance scale factor σ^2 . The intersection of the observed χ^2 (zero slope line) with a linear fit through the means of the numerically simulated probability distributions verifies the consistency of the solution residuals with the given variance-covariance matrix of the errors in the geodetic data.

from Dong [1993]) and we used both sets of uncertainties in verifying the appropriateness of the selected value of the regularization parameter, we were able to check that both sets of uncertainties are mutually consistent. Figure 7 shows the residuals versus distance from the slip centroid. We observe no significant indication of systematics with distance from the event. This again supports the use of an elastic half-space model.

We note finally that by restricting the acceptable values of the regularization parameter in this way, we obtain, in effect, solutions with no more structure than is required by the data given their a priori uncertainties. This is not to say that the true distribution of slip is not more complicated than that derived from these geodetic measurements, only that our data do not warrant further detail given these uncertainty estimates.

Geodetic Model for Slip

Plate 2 shows the inferred distribution of slip. The distribution is characterized by three main features. A large central patch of slip with a maximum value of near 0.8-m dominates the inferred model. Nearly all of the mass of the total distribution is centered on this main feature. A secondary, near-surface feature appears to the northwest with maximum slip of about 0.2 m. Finally, a small patch of slip appears to the southeast with a maximum slip of about 0.3 m. The geodetic moment derived from this distribution (computed as $\mu \sum_i s_i$, where s_i is the value of slip estimated for the i th, unit area fault element) is 1.7×10^{18} N m.

Table 2. Displacement Estimates and Postfit Residuals

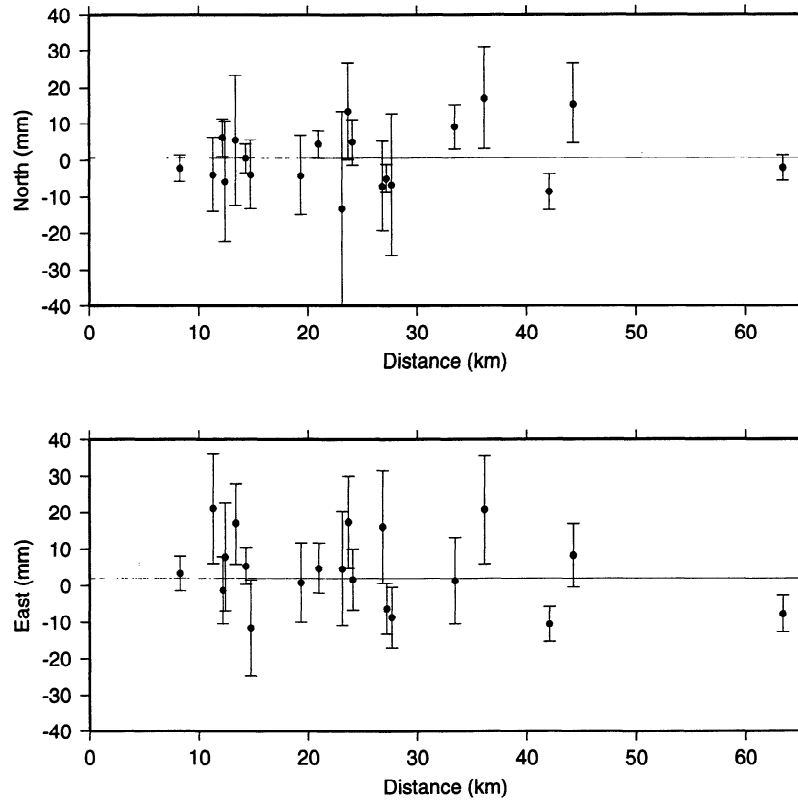
Site	Observed		Calculated		Sigma		Residuals	
	East	North	East	North	East	North	East	North
BLAC	-5.4	-3.7	2.3	-1.6	5.0	3.5	-7.7	-2.1
GARN	11.6	12.3	6.7	8.0	6.8	3.7	4.8	4.2
VIEW	21.6	-9.7	22.9	-15.9	9.1	5.2	-1.2	6.2
RAMO	19.6	19.3	14.2	18.7	5.0	3.8	5.4	0.5
COCH	0.6	-11.7	6.9	-6.7	7.0	3.8	-6.3	-4.9
WIDE	22.6	23.3	19.3	25.4	4.8	3.5	3.3	-2.1
stub	-11.7	-6.8	-1.2	1.8	4.8	5.0	-10.5	-8.6
insp	44.3	-19.8	23.2	-15.9	15.0	10.1	21.1	-3.9
berd	17.3	-21.8	12.6	-8.5	15.6	26.6	4.7	-13.3
edom	33.3	28.1	16.2	22.7	11.1	17.8	17.0	5.0
warr	-42.7	22.2	-31.1	26.1	13.2	9.4	-11.6	-3.9
keys	-15.7	-22.8	-16.6	-18.7	10.8	10.8	0.8	-4.1
quee	11.3	6.2	-6.1	-7.2	12.6	13.2	13.4	13.4
dome	5.3	6.2	-2.6	12.0	14.7	16.6	7.8	-5.8
paxn	-5.7	11.2	-7.4	6.3	8.3	6.2	1.7	4.9
mesq	-5.7	-0.2	-7.0	-9.0	11.8	6.2	1.3	9.2
palm	19.3	14.2	-1.5	-2.8	14.8	13.9	20.8	17.0
valm	4.3	11.2	-3.9	-4.3	8.7	10.9	8.2	15.5
beac	-7.7	-2.8	0.9	3.9	8.2	19.4	-8.6	-6.7
laqu	19.3	-3.8	3.2	3.3	15.4	12.2	16.1	-7.1

In millimeters.

Resolution Analysis

Uncertainty analysis for the inferred slip distribution is complicated owing to the nonlinearity of the regularization operator (due to the positivity constraint). Sim-

ilarly, Backus-Gilbert resolution analysis [Backus and Gilbert, 1968] strictly applies only to linear inverse problems. With this in mind, we investigate the response of our regularization operator numerically by running forward models and then applying the operator to the



ISDWP Residuals
One sigma ellipses (Scaled by 1.00)

Figure 7. East and north coseismic displacement residuals versus distance of the geodetic site from the slip centroid. The means (zero slope lines) are not significantly different from zero.

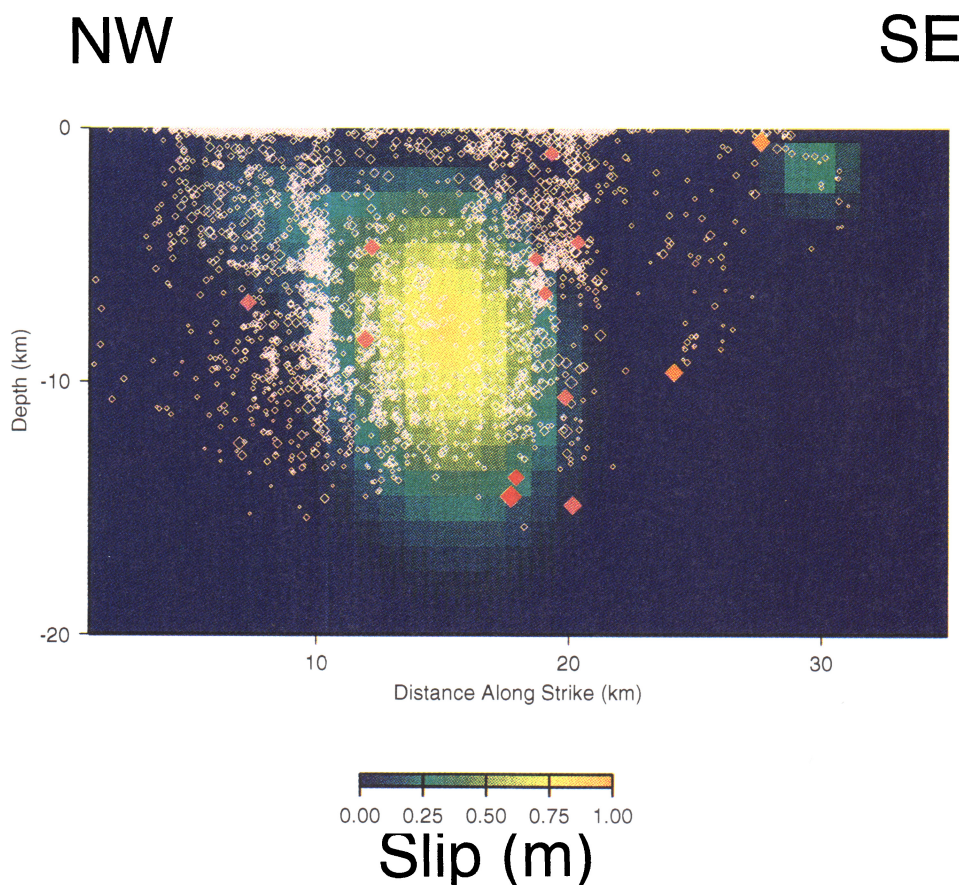


Plate 2. Slip distribution inferred from GPS and trilateration estimates of horizontal surface deformation together with aftershocks (diamonds) within 1.5 km of the fault projected onto the fault plane. The solid red diamonds indicate the location of the Joshua Tree hypocenter and foreshock. Solid pink diamonds indicate the locations of magnitude greater than four aftershocks. Orange diamonds indicate the locations of large Landers earthquake aftershocks.

resulting synthetic data. Each forward model assumed a slip distribution in which slip is concentrated at a single point, i.e., a slip impulse. We can then easily interpret three effects of imperfect resolution: location bias, amplitude bias, and smearing.

Figure 8 shows images obtained by operating on synthetic data generated from slip impulses at different locations: the centroid of our derived slip model, above this centroid, below this centroid, and at the center of the small patch of slip to the southeast of the Blue Cut fault (compare Plate 2 and Figure 8). Each of the test models has a moment of 1.7×10^{18} N m. The images have been normalized by the root sum square of the image signal. The ratio of the image to true model moments is indicated for each model.

The image centroids generally coincide with the locations of the slip impulses indicating no appreciable location bias. Even near the edges of the fault, where we expect the zero slip boundary conditions to strongly influence the solution, location bias is small. As expected, shallow slip impulses are resolved better than deeper slip impulses, as indicated by the degree of smearing.

Horizontal resolution is better than depth resolution, particularly for shallow slip. This effect appears to be less pronounced for slip impulses located near the base of the dislocation plane since the boundary conditions along the bottom of the dislocation surface affect the images of test models involving deeper slip. The ratio of image to model moments is greater than one (up to 1.23) near the surface and decreases to less than one (down to 0.80) at depth. We interpret this to result from the fact that the data do not contribute as much information at depth relative to the smoothness constraints as they do near the surface. Hence the distribution is damped more at depth than is near the surface. The fact that the moment ratio is greater than one near the surface is a result of the data “seeing” the fault at a scale smaller than that preferred given our choice of regularization parameter. (Recall that the regularization parameter was chosen based on the overall fit to the data.)

We conclude that features of the inferred model are better resolved near the surface and that the small patch of slip near the surface to the southeast is well

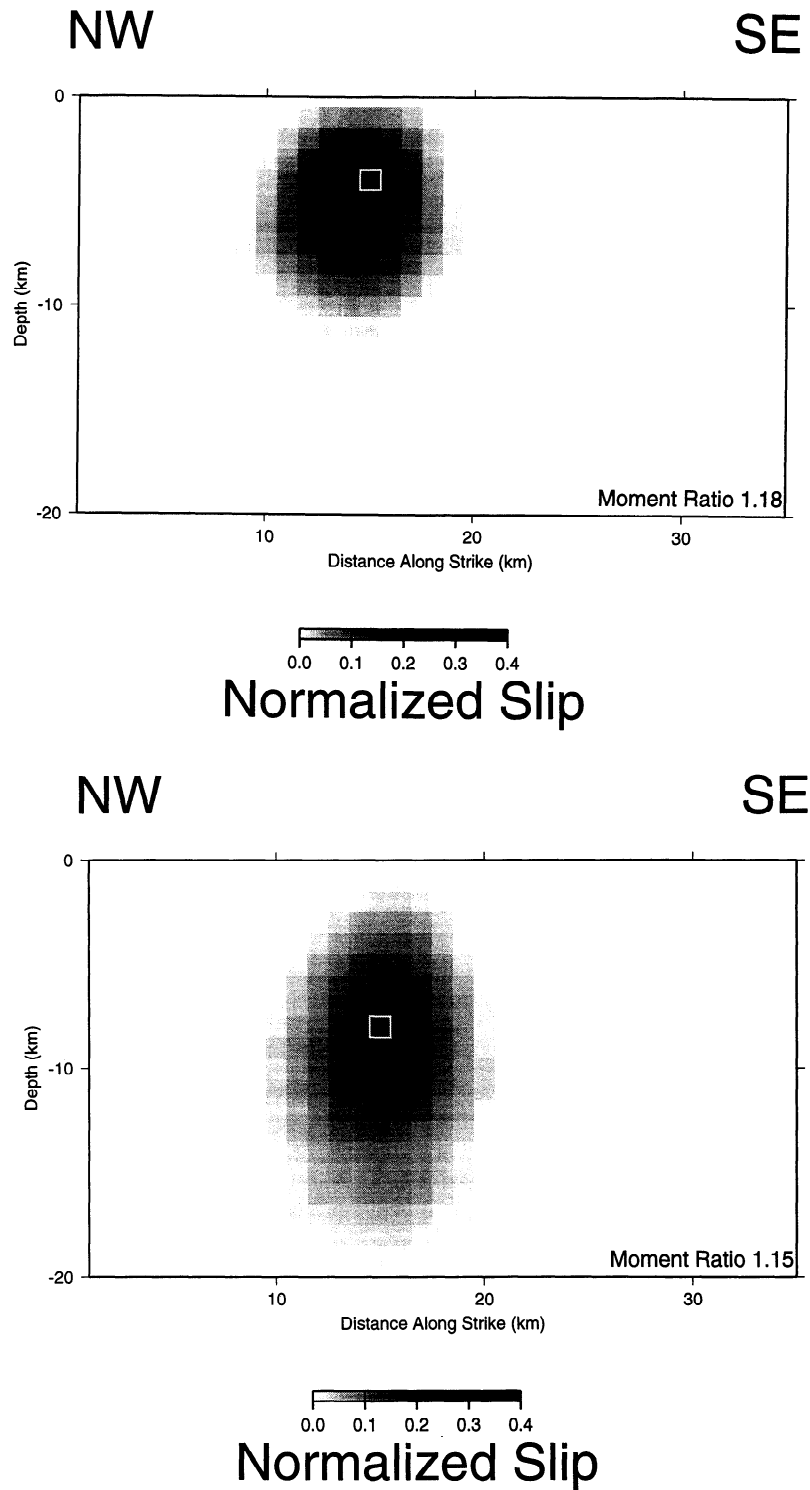


Figure 8. Normalized slip images from synthetic observations derived from slip on individual fault model elements. The ratio of the image to model moments is indicated.

resolved relative to slip on other areas of the fault. The true slip is not likely to be more spatially distributed than the inferred model, although it could very well be more localized. The location does not appear to be biased. The moment, on the other hand, may be biased by as much as 20%.

Comparison of Trilateration and GPS Data Sets

To assess the relative importance of the GPS and trilateration data sets in determining the slip distribution, we performed independent solutions using the trilateration and GPS data sets separately.

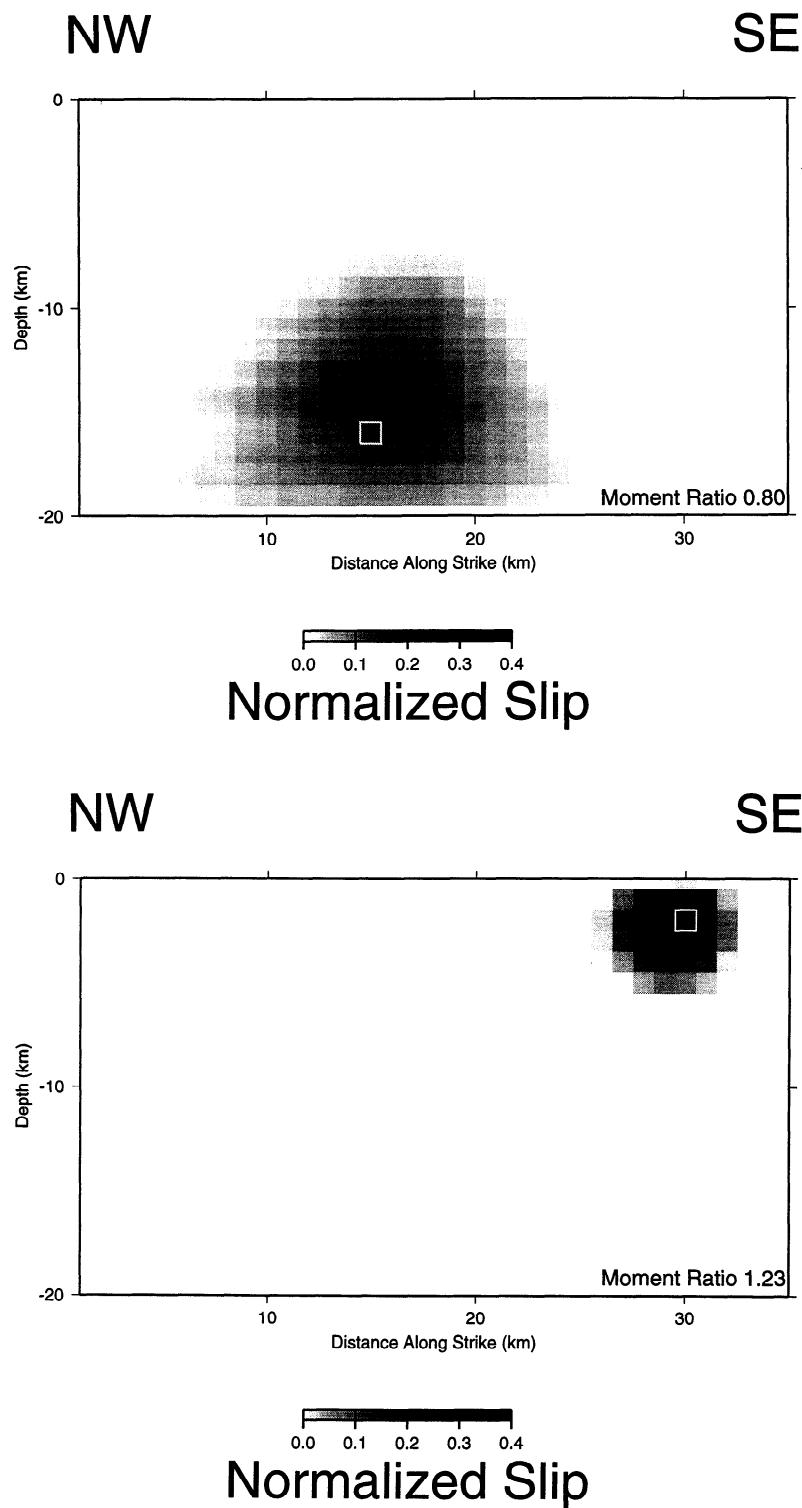


Figure 8. (continued)

The trilateration solution shown in Plate 3 is qualitatively consistent with the $7 \times 12 \text{ km}^2$ rectangular dislocation model of *Savage et al.* [1993]. However, the moment obtained from this study is near $1.4 \times 10^{18} \text{ N m}$, about 20% smaller than the *Savage et al.* model after correcting for differences in the assumed values of Earth's rigidity (we have here assumed $\mu = 28 \text{ GPa}$).

The maximum slip of our model reaches 0.76 m, comparable to the average value of 0.73 m used by *Savage et al.* [1993]. The lack of slip at depth is expected given the observed displacements at distant sites (palm, quee, stub, valm; Figure 2) which are largely incompatible with right lateral slip on the assumed fault plane.

The GPS solution is shown in Plate 4. This solution

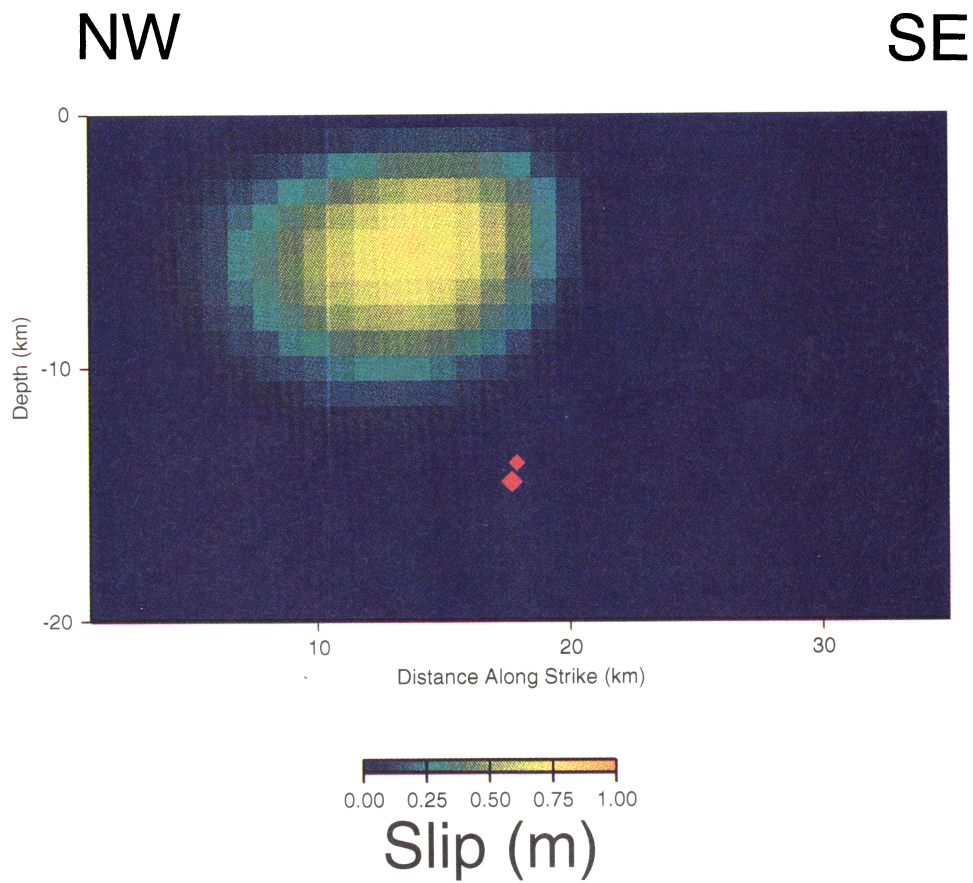


Plate 3. Slip distribution derived from trilateration data only. The solid red diamonds indicate the locations of the Joshua Tree hypocenter and foreshock.

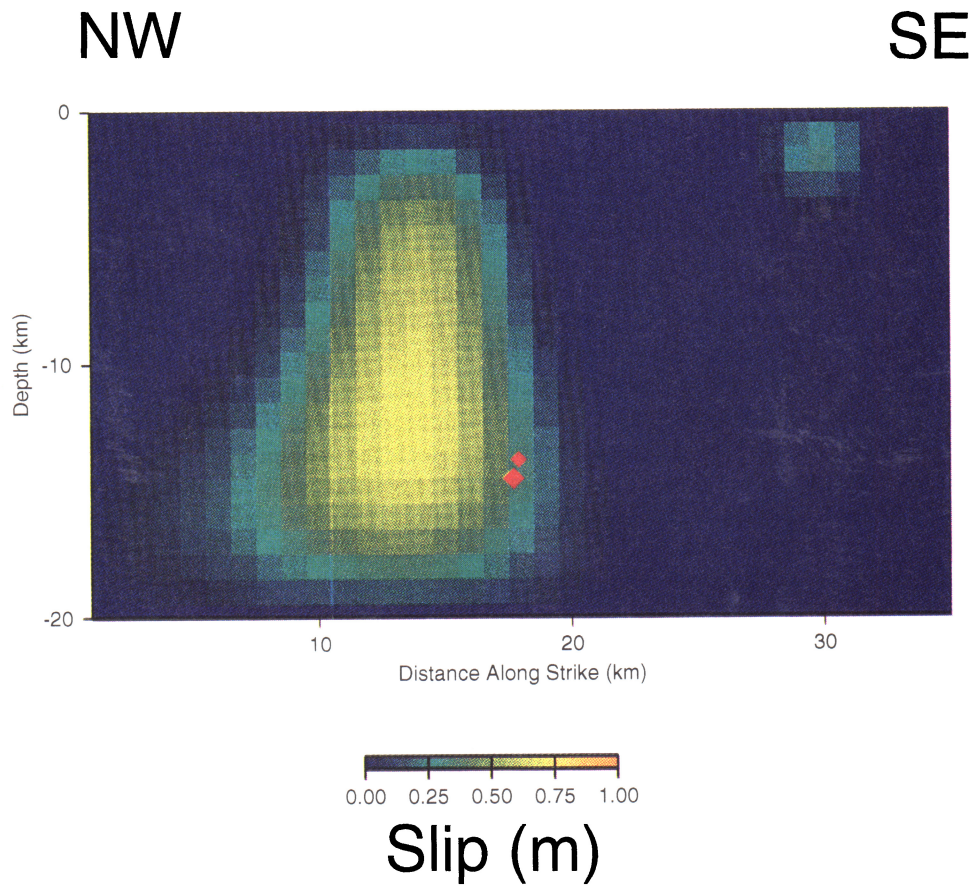


Plate 4. Slip distribution derived from GPS data only. The solid red diamonds indicate the locations of the Joshua Tree hypocenter and foreshock.

yields a moment of 2.2×10^{18} N m. There is little control of the depth extent of the slip given the GPS observations due to the sparse GPS station coverage along profiles perpendicular to the dislocation strike (Figure 2). Slip appears at depth as a result of the minimization of stress variability. The distribution is generally similar to the combined GPS and trilateration solution. The small patch of near surface slip to the southeast is clearly determined from the GPS data alone.

Independent Evidence for the Geodetically Derived Slip Model

Three primary sources of independent evidence are used to assess the significance of the inferred slip model. The main shock and aftershock hypocenters provide information about both the location and size of the rupture. In addition, seismic moment estimates provide an independent measure of the integral of slip over the dislocation surface. Last, an empirical Green's functions analysis provides estimates of the source time function of the event. The source time function provides an important estimate of rupture duration and hence of rupture size. Thus we have independent estimates of the location, magnitude, and extent of the fractured area to compare with our model for slip.

Location. In this analysis slip has been allowed to lie below 1 km depth along the specified fault plane with the lateral and depth extent of the slip completely free in the dislocation plane. The 352° striking dislocation was located so as to best coincide with the epicentral distribution of aftershocks. The centroid of the dislocation surface was placed at the intersection of the conjugate planes determined by the aftershock epicenters which roughly defines the centroid of the aftershocks (Figure 2).

The slip distribution together with the aftershock locations of Hauksson *et al.* [1993] is shown in Plate 2. The relative location of the main mass of the slip distribution and hypocenter is consistent with unilateral rupture propagation to the northwest with rupture initiating near the bottom of the fractured area. That the aftershocks tend to occur along the edges of the inferred rupture is consistent with the expected occurrence of large stress increases along these edges. This correlation is most notable for aftershocks of magnitude greater than four (Plate 2, pink diamonds).

Geodetic versus seismic moment. The geodetic moment can be obtained by integrating the slip function (Plate 2) over Σ . In the absence of positivity constraints, the moment would be expected to fluctuate with roughness. However, this is not the case for strictly positive s . While excessive damping (large regularization parameter) decreases the moment linearly with the regularization parameter (due to the homogeneous boundary conditions), the moment remains relatively constant over several orders of magnitude increase in stress variability (Figures 9 and 5).

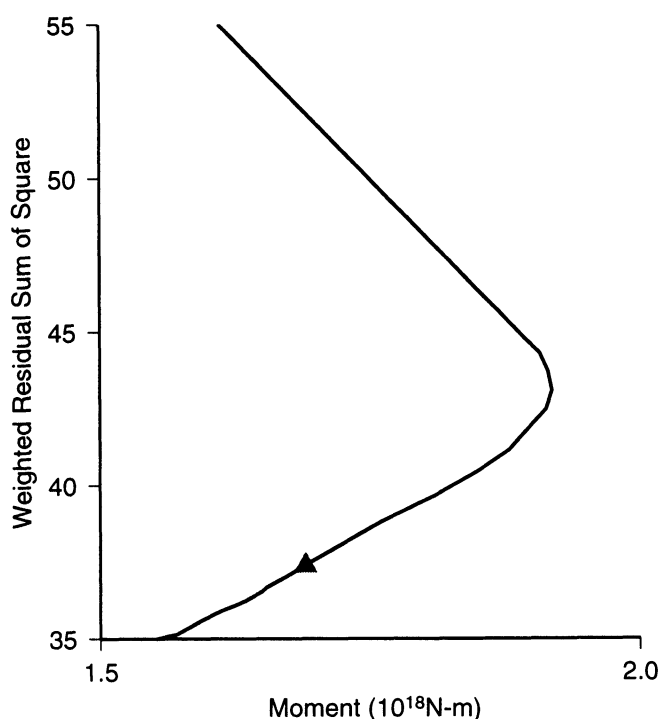


Figure 9. Geodetically derived moment versus data misfit. Triangle shows the location on the curve corresponding to the inferred model.

A moment of 1.7×10^{18} N m is estimated. This result is quite similar to that of Savage *et al.* [1993]. However, it has been pointed out that our model for slip obtained from the trilateration data alone yields a moment of only 1.4×10^{18} N m. Our estimate is slightly smaller than seismically determined moment estimates [IRIS, 1992] in the range of $1.9 - 2.4 \times 10^{18}$ N m, but these differences are not unexpected given the above mentioned moment biasing effect.

Rupture dimensions. The slip distribution presented in Plate 2 does not provide an accurate estimate of the details of the actual fractured fault. Only model averages are resolved. In order to investigate the rupture process and static stress drop, an independent estimate of source dimensions is required.

Both the Joshua Tree event and its largest aftershock (M 4.8) were well recorded by several regional seismic stations (Figure 1). Using this aftershock as a source of empirical Green's functions (eGf), the relative source time function for the Joshua Tree event was estimated (Figure 10). The source time function is impulsive and indicates a relatively simple rupture history with total rupture duration of about 5 s. Assuming a liberal range of average rupture velocities of 2.4 to 3.2 km/s, and a circular rupture area, we infer a radius in the range of 6 to 8 km. This agrees qualitatively with the distribution of slip shown in Plate 2.

Given the computed moment for the event and assuming a circular rupture with radius in the range of 6 to 8 km based on the eGf source time function, we cal-

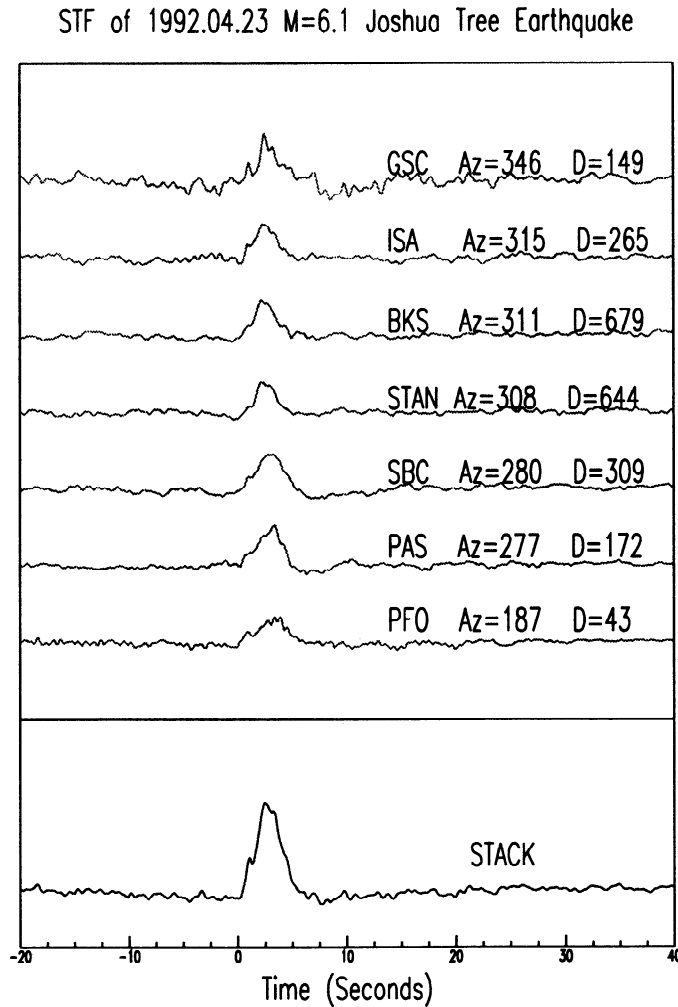


Figure 10. Source time functions for the 1992 Joshua Tree earthquake determined for each of the seismic stations shown in Figure 1 with stacked average at bottom.

culate a stress drop in the range of 2 to 4 MPa. This is significantly smaller than the estimate of 20 MPa from Lindley [1993]. However, it is well known that stress drop estimates determined by different methods can be expected to vary by up to a factor of 5 [Scholz, 1990]. The difference possibly results from complexities of the earthquake source below the resolution of our analyses, which might contribute significantly to Lindley's result. We note that to match Lindley's result given our estimated moment would require a rupture radius of about 4 km.

The source time function shown in Figure 10 provides some indication of temporal complexity in the rupture process with a small but distinct burst of energy release occurring within about 2 seconds of rupture initiation followed by the majority of the energy release. Such temporal disbursement of energy release might be indicative of spatial complexities, such as those seen in Plate 2. The variation in amplitudes of the source time functions obtained between stations GSC and PFO (Figure 10) marginally suggests rupture propagation to

the northwest, although the azimuthal distribution of stations is limited (Figure 1). This is in agreement with the hypocenter slip relationship noted above.

Earthquake-Induced Stress Changes

Coseismic stress transfer has been the subject of numerous studies [e.g., Stein and Lisowski, 1983; Stein et al., 1992; Du and Aydin, 1993; King et al. 1994]. Coseismic stress and strain changes within the half-space can be computed by differentiation of the displacement field. We assume a Poisson solid with, $\lambda = \mu = 28$ GPa. The Coulomb failure stress τ_c is then

$$\tau_c = \tau_s + \frac{3}{4}\sigma_n, \quad (16)$$

where the τ_s and σ_n are the shear and normal stress, respectively, acting on planes parallel to the dislocation surface. We have assumed an apparent coefficient of internal friction of 3/4.

Comparison of predicted Joshua Tree-induced Coulomb stress changes with the aftershock locations of

Hauksson et al. [1993] is shown in Plates 5 and 6. Plate 5 shows a horizontal cross section of stress resolved onto planes parallel to the main shock rupture plane. Plate 6 shows the same stress field on a vertical section along the main shock rupture plane. We acknowledge that the focal mechanisms of the aftershocks are not expected to coincide with that of the main shock, and we expect the effectiveness of Coulomb stress increases in bringing the brittle crust to failure to be maximal on planes optimally aligned for failure. Nevertheless, aftershocks do occur predominantly in areas for which the mainshock rupture resulted in Coulomb stress increases of greater than 0.1 MPa as computed. While the pattern of Coulomb stress changes can be modified by consideration of the direction of regional stress [e.g., *King et al.*, 1994], improvement to the correlation of aftershock occurrence with stress increases is marginal (compare with *King et al.* [1994, Figure 6]). These results support the notion that the crust must have been near failure under a relatively uniform preearthquake stress field with regional stress direction consistent with optimal right-lateral failure planes parallel to the Joshua Tree rupture plane. It is interesting to note that the largest of the Landers aftershocks to occur in the vicinity of the Joshua Tree event appear to fill in gaps in the seismicity where Joshua Tree-

induced stress increased to the southeast (Plate 6) and where stress perturbations due to the Landers earthquake would have increased the potential for failure to the northwest of the Joshua Tree rupture.

Du and Aydin [1993], in studying stress transfer along the central Calaveras fault, found that levels of earthquake-induced stress increase at the hypocenters of subsequent earthquakes along the fault are less than 5% of the static stress drop. Plate 6 shows an even smaller Joshua Tree-induced stress increase at the hypocenter of the Landers earthquake. However, about 70% of the area fractured during the Landers earthquake is thought to have sustained significant increases in Coulomb stress (0.07–0.1 MPa) prior to the event as a result of the cumulative effect of the 1975 Galaway Lake, 1979 Homestead Valley, 1986 North Palm Springs, and 1992 Joshua Tree earthquakes [*Stein et al.*, 1992; *King et al.*, 1994].

Discussion

A temporally and spatially heterogeneous process of slip along a north trending, late Quaternary fault located predominantly between the Pinto Mountain and Blue Cut faults began with the Joshua Tree earthquake (Figure 2). The generally impulsive source time function and the primary features of the slip distribution are indicative of the rupture of a single large asperity.

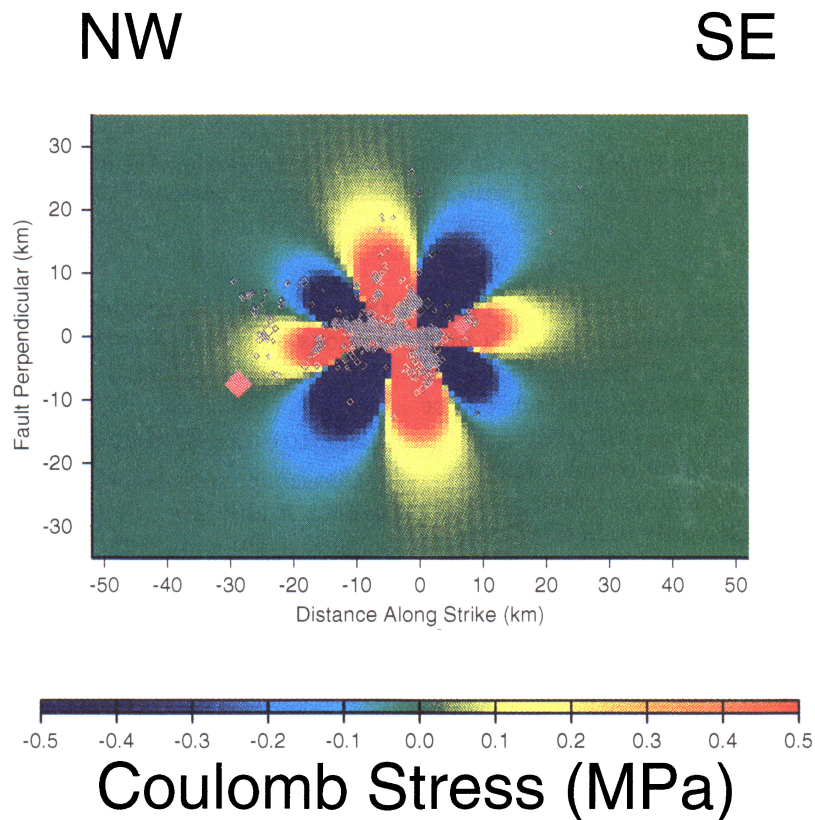


Plate 5. Predicted Coulomb failure stress changes and aftershocks (diamonds) in the depth range of 6 to 14 km projected onto a horizontal plane centered on the dislocation at 10 km depth. Solid red indicates Coulomb failure stress changes of 0.5 MPa or greater. Pink diamonds indicate location of Landers hypocenter (largest) and large of Landers aftershock.

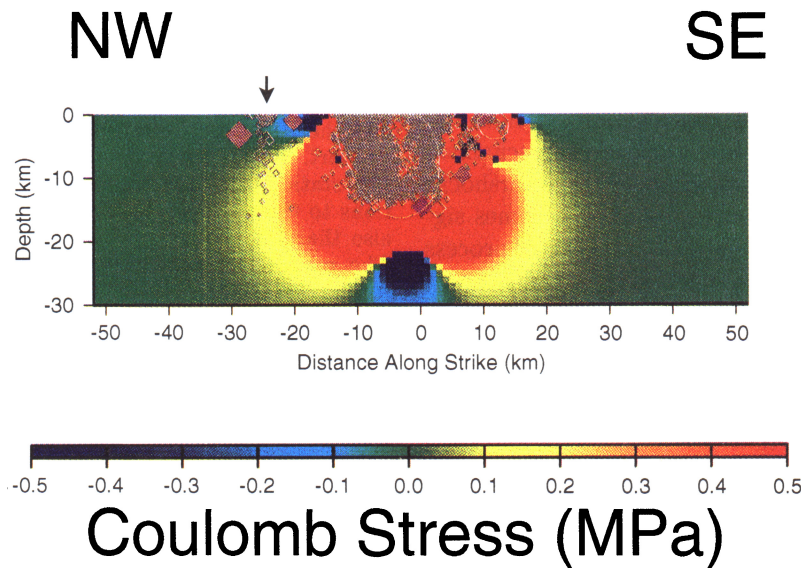


Plate 6. Predicted Coulomb failure stress changes resolved in the plane of the dislocation and aftershocks (diamonds) within 1 km of the fault projected onto the fault plane. The Joshua Tree hypocenter is shown as a dark solid diamond near the center of the figure. Lighter diamonds show the Landers hypocenter (largest) and large Landers aftershocks. Solid red indicates Coulomb failure stress changes of greater than 0.5 MPa. Arrow indicates the location of the aftershock cluster which began with the June 11 M 4.3 event. Two contour lines outline the regions of main shock slip greater than 0.01 m.

This aspect of our slip distribution is in agreement with the dislocation model of *Savage et al.* [1993]. Though resolution of finer details is limited by the nature of the Tikhonov regularization procedure, Plate 2 does suggest that smaller near surface features, one to the northwest and another to the southeast, may represent ruptures of additional asperities. The small patch of slip to the southeast lies south of the Blue Cut fault in the vicinity of mapped north trending late Quaternary faults [Clark, 1984]. Model resolution at this location is good.

Aftershocks of both the Joshua Tree and Landers earthquake appear to fill in regions along the fault plane that were not previously fractured during the sequence. Many of the largest of the Joshua Tree aftershocks occur along the southern edge of the primary patch of slip (Plate 2). The $M = 5.7$ Landers aftershock which occurred just south of the Pinto Mountain fault appears to fill in slip to the north of the Joshua Tree rupture. We conclude from these observations that the Joshua Tree earthquake and its aftershocks, as well as some large Landers aftershocks, ruptured much of the fault between the Blue Cut and Pinto Mountain faults.

The absence of significant slip and the occurrence of several aftershocks of magnitude greater than four in the vicinity of the intersection of the Blue Cut fault with the Joshua Tree main shock rupture plane (Plate 2) suggest to us that the Blue Cut fault may have largely impeded rupture propagation to the south. *Hough et al.* [1993], based on careful relocation of a $M = 5.7$ Landers aftershock, conclude that rupture associated with the Landers earthquake need not be continuous at

depth across the Pinto Mountain fault. *Hauksson et al.* [1993] observe that there appear to be no aftershocks associated with either of these two east trending left-lateral structures.

Plate 2 indicates that little slip occurred below the seismogenic cut off defined by the aftershocks with rupture initiating near the base of the slipped area. Both of these observations are in agreement with rheological models for shearing in the lithosphere [e.g., Scholz, 1988] which consider the geology of exhumed fault zones, fault rock mechanisms, rate and state dependent friction models, seismicity, and rock behavior at increased pressure and temperature. *Sibson* [1982] found that large earthquakes tend to nucleate near the base of the seismogenic zone, a region of high shear resistance and strain energy concentration. A relevant exception, however, is the Landers earthquake which initiated at very shallow depth.

The coseismic stress increase predicted at the hypocenter of the June 28, 1992, Landers event due to the Joshua Tree earthquake is near zero (Plate 6). We conclude, then, that the Landers event was not directly triggered by coseismic stress increase associated with the Joshua Tree rupture. However, migration of aftershocks to the northwest in the months following the Joshua Tree event is illustrated by the occurrence of a small cluster about 20 km beyond the northern edge of Joshua Tree slip (Plate 6, arrow). This cluster began with a $M = 4.3$ aftershock on June 11 near 7 km depth within about 10 km of the June 28 Landers hypocenter. Predicted Joshua Tree-induced Coulomb stress increase

at the hypocenter of this $M = 4.3$ aftershock is near 0.06 MPa (Plate 6).

Clearly, the spatial correlation of aftershocks and Coulomb stress changes indicates a causal relationship. Less clear, however, is the time dependent mechanism through which these changes produce the aftershocks and the level at which the stress increase becomes significant. We may only speculate as to the exact process or combination of processes which lead to the Landers earthquake. Nevertheless, the close proximity in space and time of the Joshua Tree and Landers earthquakes, their occurrence on virtually the same fault, and migration of Joshua Tree earthquake aftershocks to the northwest suggest to us that the Joshua Tree and Landers earthquakes are part of a single northwest propagating rupture process.

Conclusion

We have used geodetically derived estimates of coseismic displacement at 20 sites to infer the slip distribution and static stress transfer associated with the April 23, 1992, Joshua Tree, California, earthquake. Source parameter estimates obtained by application of a Tikhonov regularization operator agree well with independent estimates from seismic studies. The estimated geodetic moment is 1.7×10^{18} N m. The source time function inferred from empirical Green's function analyses indicates a rupture duration of about 5 s. Assuming a circular rupture yields a fracture radius in the range of 6 to 8 km. The stress drop is in the range of 2 to 4 MPa. The Joshua Tree event involved rupture of at least one asperity with the possibility of minor amounts of slip occurring near the surface to the north of the main slip patch, and also to the south of the Blue Cut fault. The fit between observed and predicted ground motions, location of the rupture relative to the hypocenter, a strong correlation of the aftershock locations and predicted stress change patterns, and qualitative agreement of source time function and static coseismic slip provide strong support for the geodetically derived slip distribution.

For the Joshua Tree event, aftershock activity is highly correlated with Coulomb stress increases of greater than about 0.1 MPa. This supports the notion that the brittle crust in this area was near failure under a relatively uniform preearthquake stress field. Stress increase predicted at the hypocenter of the Landers earthquake is near zero implying that the Landers event was not directly triggered by coseismic stress changes. We speculate that redistribution of Joshua Tree-induced stress perturbations during the two months following the Joshua Tree event could explain the temporal development of the earthquake sequence culminating in the M_w 7.3, June 28, 1992, Landers event. In particular, we suggest that the Joshua Tree and Landers earthquakes are part of a single northwest propagating rupture process.

Acknowledgments. This work would not have been possible were it not for the considerable field efforts of a host of people from various universities, and state and county agencies. In particular, we would like to thank Bill Young and the Riverside County Flood Control District for their support. We are grateful to D. Dong for providing trilateration station displacement estimates and for many contributions to the geodetic data processing software at MIT. We also thank E. Hauksson for providing aftershock locations. The manuscript benefited substantially from constructive comments of R. W. King and two anonymous reviewers. This work was funded by USGS grant 1424-92-G-2162 and NASA grant NAG5-2206 through the Carnegie Institution of Washington. Special thanks to Liz Henderson at the Earth Resources Laboratory for typesetting the manuscript.

References

- Aki, K., and P. G. Richards, *Quantitative Seismology: Theory and Methods*, vol. 1, W. H. Freeman, New York, 1980.
- Backus, G., and F. Gilbert, The resolving power of gross Earth data, *Geophys. J. R. Astron. Soc. Am.*, **16**, 169–205, 1968.
- Ben-Menahem, A., and A. Gillon, Crustal deformation by earthquakes and explosions, *Bull. Seismol. Soc. Am.*, **60**, 193–215, 1970.
- Ben-Menahem, A., and S. J. Singh, Multipolar elastic fields in a layered half space, *Bull. Seismol. Soc. Am.*, **58**, 1519–1572, 1968.
- Ben-Menahem, A., S. J. Singh, and S. J. Solomon, Deformation of a homogeneous Earth model by finite dislocations, *Rev. Geophys.*, **8**, 591–632, 1970.
- Chinnery, M. A., The deformation of the ground around surface faults, *Bull. Seismol. Soc. Am.*, **51**, 335–372, 1961.
- Clark, M. M., Map showing recently active breaks along the San Andreas fault and associated faults between Salton Sea and Whitewater River-Mossion Creek, California, scale 1:24000, *U.S. Geol. Surv., Misc. Invest. Ser., Map I-1483*, 2 sheets, 1984.
- Dokka, R. K., and C. J. Travis, Late Cenozoic strike-slip faulting in the Mojave desert, California, *Tectonics*, **9**, 311–340, 1990a.
- Dokka, R. K., and C. J. Travis, Role of the eastern California Shear Zone in accommodating Pacific-North American plate motion, *Geophys. Res. Lett.*, **17**, 1323–1326, 1990b.
- Dong, D., The horizontal velocity field in southern California from a combination of terrestrial and space geodetic data, Ph.D thesis, Mass. Inst. of Technol., Cambridge, 1993.
- Du, Y., and A. Aydin, Stress transfer during three sequential moderate earthquakes along the central Calaveras fault California, *J. Geophys. Res.*, **98**, 9947–9962, 1993.
- Du, Y., A. Aydin, and P. Segall, Comparison of various inversion techniques as applied to the determination of a geophysical deformation model for the Borah Peak earthquake, *Bull. Seismol. Soc. Am.*, **82**, 1840–1866, 1992.
- Feigl, K.L., et al., Space geodetic measurement of crustal deformation in central and southern California, 1984–1992, *J. Geophys. Res.*, **98**, 21,677–21,712, 1993.
- Hartzell, S.H. and T.H. Heaton, Inversion of strong ground motion and teleseismic waveform data for the fault rupture history of the 1979 Imperial Valley, California, earthquake, *Bull. Seismol. Soc. Am.*, **73**, 1553–1583, 1983.
- Hauksson, E., L. M. Jones, K. Hutton, and D. Eberhart-Phillips, The Landers earthquake sequence: Seismological observations, *J. Geophys. Res.*, **98**, 19,835–19,858, 1993.
- Hough, S. E., J. Mori, E. Sembera, G. Glassmoyer, C. Mueller, and S. Lydeen, Southern surface rupture associated with the 1992 M 7.4 Landers earthquake: Did it

- all happen during the mainshock?, *Geophys. Res. Lett.*, **20**, 2615–2618, 1993.
- Incorporated Research Institutions for Seismology (IRIS), Data Management Center Electronic Bulletin Board, Univ. of Wash., Seattle, 1992.
- Jovanovich, D. B., M. I. Husseini, and M. A. Chinnery, Elastic dislocations in a layered half-space, I, Basic theory and numerical methods, *Geophys. J. R. Astron. Soc.*, **39**, 205–217, 1974a.
- Jovanovich, D. B., M. I. Husseini, and M. A. Chinnery, Elastic dislocations in a layered half-space, II, The point source, *Geophys. J. R. Astron. Soc.*, **39**, 219–239, 1974b.
- King, G. C., R. S. Stein, and J. Lin, Static stress changes and the triggering of earthquakes, *Bull. Seismol. Soc. Am.*, **84**, 935–953, 1994.
- Larsen, S., R. Reilinger, H. Neugebauer, and W. Strange, Global Positioning System measurements of deformations associated with the 1987 Superstition Hills earthquake: Evidence for conjugate faulting, *J. Geophys. Res.*, **97**, 4885–4902, 1992.
- Lawson, C. L., and R. J. Hanson, *Solving Least Squares Problems*, Prentice Hall, Englewood Cliffs, N.J., 1974.
- Lindley, G. T., Source parameters of the 23 April 1992 Joshua Tree, California, earthquake, its largest foreshock, and aftershocks, *Eos Trans. AGU*, **74**(43), Fall Meeting suppl., 397, 1993.
- Mansinha, L., and D.E. Smylie, Displacement fields of inclined faults, *Bull. Seismol. Soc. Am.*, **61**, 1433–1440, 1971.
- Matthews, M., Fault slip in space and time, Ph.D. thesis, Stanford Univ., Stanford, Calif., 1991.
- Mendoza, C. and S. H. Hartzell, Inversion for slip distribution using teleseismic *P* waveforms: North Palm Springs, Borah Peak, and Michoacan earthquakes, *Bull. Seismol. Soc. Am.*, **78**, 1092–1111, 1988.
- Morozov, V. A., *Regularization Methods for Ill-Posed Problems*, 257 pp., CRC Press, Boca Raton, FL, 1993.
- Murray, M. H., J. C. Savage, M. Lisowski, and W. K. Gross, Coseismic displacements: 1992 Landers, California, earthquake, *Geophys. Res. Lett.*, **20**, 623–626, 1993.
- Nur, A., H. Ron, G. Beroza, and L. Alfonsi, A fault is born: The mechanical origin of the Mojave seismic line, *Eos Trans. AGU*, **73**(43), Fall Meeting suppl., 362, 1992.
- Okada, Y., Surface deformation due to shear and tensile faults in a half space, *Bull. Seismol. Soc. Am.*, **75**, 1135–1154, 1985.
- Reilinger, R., and S. Larsen, Present-day crustal deformation in the Salton Trough, southern California, in *Contributions of Space Geodesy to Geodynamics: Crustal Dynamics, Geodyn. Ser.*, vol. 23, edited by D. E. Smith and D. L. Turcotte, pp. 177–192, AGU, Washington, D.C., 1993.
- Richter, C. F., C. R. Allen, and J. M. Nordquist, The Desert Hot Springs earthquakes and their tectonic environment, *Bull. Seismol. Soc. Am.*, **48**, 315–337, 1958.
- Rymer, M. J., The 1992 Joshua Tree, California, earthquake: Tectonic setting and triggered slip (abstract), *Eos Trans. AGU*, **73**(43), Fall Meeting suppl., 363, 1992.
- Sauber, J., W. Thatcher, and S. C. Solomon, Geodetic measurement of deformation in the central Mojave desert, California, *J. Geophys. Res.*, **91**, 12,683–12,693, 1986.
- Savage, J. C., Effect of crustal layering upon dislocation modeling, *J. Geophys. Res.*, **92**, 10,595–10,600, 1987.
- Savage, J. C., and L. M. Hastie, Surface deformation associated with dip-slip faulting, *J. Geophys. Res.*, **71**, 4897–4904, 1966.
- Savage, J. C., M. Lisowski, and W. Prescott, An apparent shear zone trending north-northwest across the Mojave desert into Owens Valley, eastern California, *Geophys. Res. Lett.*, **17**, 2113–2116, 1990.
- Savage, J. C., M. Lisowski, and M. Murray, Deformation from 1973 through 1991 in the epicentral area of the 1992 Landers, California, earthquake ($M_s = 7.5$), *J. Geophys. Res.*, **98**, 19,951–19,958, 1993.
- Scholz, C.H., The brittle-plastic transition and the depth of seismic faulting, *Geol. Rundsch.*, **77**, 317–328, 1988.
- Scholz, C.H., *The Mechanics of Earthquakes and Faulting*, 439 pp., Cambridge University Press, New York, 1990.
- Segall, P., and R. Harris, Earthquake deformation cycle on the San Andreas fault near Parkfield, California, *J. Geophys. Res.*, **92**, 10,511–10,525, 1987.
- Sibson, R., Fault zone models, heat flow, and depth distribution of earthquakes in the continental crust of the United States, *Bull. Seismol. Soc. Am.*, **72**, 151–163, 1982.
- Sieh, K. S., and P. L. Williams, Behavior of the southernmost San Andreas fault during the past 300 years, *J. Geophys. Res.*, **95**, 6629–6645, 1990.
- Sieh, K., M. Stuiver, and D. Brillinger, A more precise chronology of earthquakes produced by the San Andreas fault in southern California, *J. Geophys. Res.*, **94**, 603–623, 1989.
- Singh, S., J., Static deformation of a multilayered half-space by internal sources, *J. Geophys. Res.*, **75**, 3257–3263, 1970.
- Stein, R. S., and M. Lisowski, The 1979 Homestead Valley earthquake sequence, California: Control of aftershocks and postseismic deformation, *J. Geophys. Res.*, **88**, 6477–6490, 1983.
- Stein, R. S., G. C. King, and J. Lin, Changes in failure stress on the southern San Andreas fault system caused by the 1992 magnitude = 7.4 Landers earthquake, *Science*, **258**, 1328–1332, 1992.
- Steketee, J. A., On Volterra's dislocations in a semi-infinite elastic medium, *Can. J. Phys.*, **36**, 192–205, 1958a.
- Steketee, J. A., Some geophysical applications of the elasticity theory of dislocations, *Can. J. Phys.*, **36**, 1168–1198, 1958b.
- Sykes, L. R., and L. Seeber, Great earthquakes and great asperities, San Andreas fault, southern California, *Geology*, **13**, 835–838, 1985.
- Tikhonov, A. N., and V. Y. Arsenin, *Solutions to Ill-Posed Problems*, V. H. Winston, Washington, D. C., 1977.
- Wahba, G., Spline models for observational data, paper presented at CBMS-NSF Regional Conference Series in Applied Mathematics, Soc. for Ind. and Appl. Math., Philadelphia, Pa., 1990.
- Wald, D. J., and T. H. Heaton, Spatial and temporal distribution of slip for the 1992 Landers, California earthquake, *Bull. Seismol. Soc. Am.*, **84**, 668–691, 1994.
- Ward, S. N., and S. E. Barrientos, An inversion for slip distribution and fault shape from geodetic observations of the 1983, Borah Peak, Idaho, earthquake, *J. Geophys. Res.*, **91**, 4909–4919, 1986.

R. A. Bennett, Y. Li, R. E. Reilinger, W. Rodi, and M. N. Toksöz, Earth Resources Laboratory, Department of Earth, Atmospheric, and Planetary Sciences, Massachusetts Institute of Technology, 42 Carleton Street, Cambridge MA 02142-1324. (e-mail: bennett@erl.mit.edu)

K. Hudnut, U.S. Geological Survey, 525 South Wilson Ave., Pasadena, CA 91106.

(Received March 11, 1994; revised November 7, 1994; accepted November 8, 1994.)